PARABOLIC APPROXIMATIONS FOR WATER WAVES IN CONFORMAL COORDINATE SYSTEMS

James T. Kirby, Robert A. Dalrymple and Haruhiko Kaku

RESEARCH REPORT NO. CACR-94-03

January 1994

CENTER FOR APPLIED COASTAL RESEARCH
Ocean Engineering Laboratory
University of Delaware
Newark, Delaware 19716

Parabolic Approximations for Water Waves in Conformal Coordinate Systems

James T. Kirby and Robert A. Dalrymple
Center for Applied Coastal Research, Department of Civil Engineering
University of Delaware, Newark, DE 19716

Haruhiko Kaku
Deck Inc., Ohnuki Bldg. 604
2-47 Miyagawa-cho, Naka-ku, Yokohama 231 Japan

Abstract

A general formulation of small and large-angle parabolic approximations in conformally mapped coordinate systems is introduced. The technique is applied to the study of two particular cases involving a polar coordinate system. Comparisons to data and full solutions of the governing Helmholtz equation are given. For the case of waves between diverging breakwaters, we find that distinct differences exist between the lowest order parabolic approximation and an analytic solution in the Kirchoff approximation in polar coordinates. The errors are only partially alleviated in the next higher order approximation. For the case of waves in a circular channel bend, we find a similar level of disagreement between lowest-order parabolic approximations and full solutions. The higher order approximation produces results which are reasonably accurate in this case. In both cases, we also investigate the effects of wave nonlinearity, and investigate the growth of Mach stems at the outer wall of circular channel bends.

1 Introduction

The parabolic equation method for surface water wave propagation has undergone rapid development recently as a method for computing the forward scattering and combined refraction-diffraction of waves in the coastal environment. Both Cartesian coordinate methods and methods based on curvilinear coordinates tied to a background refraction problem have been extensively developed. A review of existing Cartesian methods may be found in Liu (1990).

Coastal areas often contain structures such as jetties and breakwaters that intersect a pre-chosen Cartesian computational grid at large angles to coordinate lines. The resulting internal boundaries are then difficult to accommodate in the finite-difference coding.

Primarily for this reason, interest in the application of boundary-fitted grid systems has recently developed. These systems have the effect of reducing internal structures to lateral boundaries in the forward-marching solution technique. Results to date have concentrated on idealized situations involving simple boundary configurations (for example, Liu and Boissevain (1988) and Kirby (1988)), but application of generalized boundary-fitting techniques is sure to follow (see, for example, Thompson *et al*, 1985). Liu and Boissevain (1988) reported a non-conformal transformation for waves between two breakwaters, which proceeds by transforming the Cartesian parabolic approximation into the boundary-conforming grid system. Kirby (1988) re-examined Liu and Boissevain's model and has shown that the more consistent procedure of mapping the full governing equations by the coordinate transformation, followed by the construction of the parabolic approximation in the transformed space, provides a more logical and accurate means of predicting the wave field.

Here, we concentrate on conformal coordinate transformations. In Section 2, we take the mild slope equation for strictly monochromatic wave propagation (Berkhoff, 1972) through a generalized coordinate transformation, and then restrict the resulting model to the case where the transformation is conformal. Parabolic equations corresponding to the usual lowest-order approximation are then constructed for the conformal and general case. We further construct the next higher-order approximation for the conformal case, following Booij (1981) and Kirby (1986). We note that lowest-order approximations have been previously presented for several geometries by Tsay *et al* (1989); however, their results were not consistent with earlier (successful) calculations on regular grids for the geometries considered, and hence there is still ample room for the development of the modeling schemes.

In Sections 3 and 4, we consider the application of the models in two instances where the domain boundaries are easily specified in a polar coordinate system. In Section 3, we consider waves propagating between a pair of diverging breakwaters, where the boundaries lie along lines of constant angle θ. Nonlinear effects appropriate to monochromatic Stokes waves are included following Kirby and Dalrymple (1984). Computational examples and comparisons with experimental results are given.

In Section 4, we consider the propagation of initially plane waves around a channel bend contained between two curved sidewalls of fixed radius. The small and large-angle parabolic models are compared to an analytic solution, which shows that the large-angle model provides an accurate prediction of the wave field in the bend. We then examine the effect of wave nonlinearity and study the evolution of a Mach stem reflection along the outer wall. Qualitative comparisons are made to previous experimental results of Nielsen (1962), which were obtained with a slightly different geometry.

2 Coordinate Transformations and Parabolic Approximations

We take the mild-slope equation of Berkhoff (1972), governing the instantaneous water surface displacement $\eta(x, y)$, as our starting point:

$$(CC_g\eta_x)_x + (CC_g\eta_y)_y + k^2CC_g\eta = 0. \tag{1}$$

Here, subscripts denote derivatives, the wavenumber k is related to the local water depth h by the dispersion relation

$$\omega^2 = gk \tanh kh, \tag{2}$$

g is gravitational acceleration, and ω is the wave angular frequency. The water motion is assumed to be purely harmonic in time. The remaining coefficients are phase speed $C = \omega/k$ and group velocity $C_g = \partial\omega/\partial k$; both of which vary with the water depth.

To justify parabolic approximations, which are based on assuming that the principal propagation direction is the x direction, we use the multiple scales method. Considering only the constant depth case for simplicity, we introduce the multiple scales according to

$$\begin{aligned} x &\rightarrow \delta^0 x + \delta x + \delta^2 x + \ldots = x_0 + x_1 + x_2 + \ldots \\ y &\rightarrow \delta^0 y + \delta y + \delta^2 y + \ldots = y_0 + y_1 + y_2 + \ldots \end{aligned} \tag{3}$$

where $\delta \ll 1$. We assume η to be of the form

$$\eta = Re\{A(x_1, x_2, y_1, y_2, \ldots)\, \mathrm{e}^{ikx}\} \tag{4}$$

where no fast-scale variation in y is permitted. Substituting (3) and (4) into (1) and ordering by powers of δ leads to:

$$O(\delta) \ : \qquad A_{x_1} = 0 \tag{5}$$

$$O(\delta^2) \ : \qquad 2ikA_{x_2} + A_{y_1y_1} = 0 \tag{6}$$

Equation (6) is then the lowest order parabolic approximation, and implies that A has at most a dependence on x_2 at $O(\delta^2)$. This approximation implies scale relations between derivatives of the amplitude of the form

$$\begin{aligned} A_x/A_y &= O(\delta) \\ kA_x/A_{xx} &= O(\delta^{-2}) \end{aligned} \tag{7}$$

when scales are not made apparent. Since A_{xx} is small with respect to the first derivative terms, it may be dropped.

2.1 Parabolic Approximations in Other Coordinate Systems

We first reduce the mild-slope equation to a variable-coefficient Helmholtz equation, by introducing a transformation described by Radder (1979), which is

$$\Phi = \sqrt{CC_g}\eta, \tag{8}$$

into the mild-slope equation giving us

$$\Phi_{xx} + \Phi_{yy} + K^2\Phi = 0 \tag{9}$$

where

$$K^2 = k^2 - \frac{(\sqrt{CC_g})_{xx} + (\sqrt{CC_g})_{yy}}{\sqrt{CC_g}} \tag{10}$$

Consider mappings of the variable-coefficient Helmholtz equation from Cartesian $\{x, y\}$ space into an alternate $\{u, v\}$ space, where the mapping may or may not be conformal. We take

$$\begin{pmatrix} x \\ y \end{pmatrix} = \begin{pmatrix} x(u,v) \\ y(u,v) \end{pmatrix}, \text{ or } \begin{pmatrix} u \\ v \end{pmatrix} = \begin{pmatrix} u(x,y) \\ v(x,y) \end{pmatrix} \tag{11}$$

The mapping is presumed to be one-to-one in the domain of relevant fluid motion, and on boundaries of that domain. The first form of (11) will typically be used below.

From the chain rule, we can write partial derivatives in the following way:

$$\Phi_x = \Phi_u u_x + \Phi_v v_x \tag{12}$$

$$\Phi_y = \Phi_u u_y + \Phi_v v_y \tag{13}$$

Applying these operators again to obtain second derivatives and then applying these to the governing equation (9) yields

$$\left(u_x^2 + u_y^2\right)\Phi_{uu} + 2\left(u_x v_x + u_y v_y\right)\Phi_{uv} + \left(v_x^2 + v_y^2\right)\Phi_{vv} + \nabla^2 u\Phi_u + \nabla^2 v\,\Phi_v + K^2\Phi = 0 \quad (14)$$

While the derivatives of Φ above are taken with respect to the mapped coordinates, the coefficients of the derivatives still involve the derivatives of u and v with respect to x and y. To change this, we apply the chain rule derivative operator for x to the elemental lengths dx and dy,

$$\begin{aligned} 1 &= x_u u_x + x_v v_x && (15) \\ 0 &= y_u u_x + y_v v_x && (16) \end{aligned}$$

This set of linear equations is easily solved for u_x and v_x:

$$\begin{aligned} u_x &= \frac{1}{J} y_v && (17) \\ v_x &= -\frac{1}{J} y_u; \qquad J = x_u y_v - x_v y_u && (18) \end{aligned}$$

where J is the Jacobian of the transformation. Using the y derivative operator applied to dx and dy results in

$$\begin{aligned} u_y &= -\frac{1}{J} x_v && (19) \\ v_y &= \frac{1}{J} x_u && (20) \end{aligned}$$

Utilizing these definitions in the coefficients of (14) yields the transformed Helmholz equation:

$$\alpha\Phi_{uu} - 2\gamma\Phi_{uv} + \beta\Phi_{vv} + J^2\{(\nabla^2 u)\Phi_u + (\nabla^2 v)\Phi_v + K^2\Phi\} = 0 \quad (21)$$

where

$$\begin{aligned} \alpha &= x_v^2 + y_v^2 \\ \beta &= x_u^2 + y_u^2 \\ \gamma &= x_u x_v + y_u y_v && (22) \end{aligned}$$

Expressions for $\nabla^2 u$ and $\nabla^2 v$ are given in Appendix A. The case of a general transformation may take the Helmholtz equation into an equation with first derivatives and a cross-derivative term; however, (21) may be shown to be elliptic in all cases (Thompson *et al.*, 1985).

For the special case of a conformal transformation, we make use of the Cauchy-Riemann conditions:

$$\begin{aligned} x_u &= y_v \\ x_v &= -y_u \end{aligned} \tag{23}$$

to obtain

$$\nabla^2 u = \nabla^2 v = \gamma = 0 \tag{24}$$

and

$$\alpha = \beta = J(u, v) \tag{25}$$

Eq. (21) then reduces to

$$\Phi_{uu} + \Phi_{vv} + K^2 J(u, v)\Phi = 0, \tag{26}$$

which is our governing equation in the conformal domain.

Turning to the construction of parabolic approximations, we may assume that the wave being considered consists of a progressive wave whose phase accumulates along lines of constant v, and which therefore has u as the preferred propagation direction. We may then write $\Phi(u, v)$ in the form

$$\Phi(u, v) = Re\left\{A(u, v)\mathrm{e}^{i\int KJ^{1/2}du}\right\} \tag{27}$$

where the factor $KJ^{1/2}$ in the phase accounts for the proper accumulation of physical distance as the wave propagates. Since $K(u, v)$ and $J(u, v)$ still vary with v, it is convenient to define a reference phase function based on $K(u, v_0) = K_0(u)$ and $J(u, v_0) = J_0(u)$; i.e., the phase function for one particular line $v = v_0$. We then substitute $K_0 J_0^{1/2}$ in (27) in place of $KJ^{1/2}$. For this case, substituting our assumed form for Φ (27) into (26) produces the parabolic approximation

$$2iK_0J_0^{1/2}A_u + i(K_0J_0^{1/2})_uA + (K^2J - K_0^2J_0)A + A_{vv} = 0 \tag{28}$$

after neglecting the small term A_{uu}. The scale relations between u and v derivatives in (28) are essentially identical to the relations in (6), and we see that taking the Helmholtz equation through a conformal mapping poses no problems in interpreting parabolic approximations constructed in the mapped space.

In contrast, substituting (27) into the general form of the Helmholz equation (21) leads to the complicated envelope equation

$$\begin{aligned}(\alpha A_{uu} - 2\gamma A_{uv} + JA_{vv}) + \left(2i\alpha K_0J_0^{1/2} + J^2(\nabla^2 u)\right)A_u + \left(-2i\gamma K_0J_0^{1/2} + J^2(\nabla^2 v)\right)A_v +\\ \left\{K^2J^2 - \alpha J_0K_0^2 + i\alpha(K_0J_0^{1/2})_u + iJ^2(\nabla^2 u)K_0J_0^{1/2}\right\}A = 0(29)\end{aligned}$$

A quasi-parabolic equation may be simply constructed by dropping the A_{uu} term again, and the resulting equation poses no problem as a computational system, using standard implicit techniques for parabolic equations (see Kirby (1988) for a particular non-conformal case). However, the remaining terms may not be scaled in an entirely consistent manner, due to the loss of conformal correspondence with the original Cartesian physical space.

The problem of correspondence between solutions of non-conformal parabolic systems of the form (29) and solutions of the original Helmholtz equation will require a great deal of attention as the modelling systems evolve. We restrict our attention in the remainder of this study to the conformal case, which constitutes a necessary part of the groundwork for later studies.

We note that an alternate form of (28) which more closely corresponds to the following section may be constructed by first using the form (27) retaining $J(u, v)$ to reduce u-derivative terms, after which the shift to the J_0 form is made in order to reduce v-derivative terms. The resulting model is given by

$$2iKJ^{1/2}A_u + i(KJ^{1/2})_uA + 2KJ^{1/2}(KJ^{1/2} - K_0J_0^{1/2})A + A_{vv} = 0 \tag{30}$$

The forms (28) and (30) are equivalent for the polar transformation of Section 3.

2.2 Large-angle Parabolic Approximations

The parabolic model developed in the previous section represents the so-called lowest-order approximation to the general problem of waves propagating forward with respect to a specified coordinate u. Various methods exist for constructing higher-order approximations which allow a greater deviation between the preferred coordinate and the local direction of propagation. Here, a method proposed by Booij (1981) is utilized to construct the higher-order (or large-angle) approximation. Booij's method has been justified previously in the context of a consistent multiple-scale expansion by Kirby (1986).

We wish to split the governing Helmholtz equation (26) into equations for forward and back-scattered waves Φ^+ and Φ^-, where $\Phi = \Phi^+ + \Phi^-$. Booij showed that an associated equation

$$\left(\sigma^{-1}\phi_{m,u}\right)_u + \sigma\phi_m = 0 \tag{31}$$

is split identically into

$$\begin{aligned} (\phi_m^+)_u &= i\sigma\phi_m^+ \\ (\phi_m^-)_u &= -i\sigma\phi_m^- \end{aligned} \tag{32}$$

where $\phi_m^+ + \phi_m^- = \phi_m$. We proceed by defining

$$\phi_m = \lambda\Phi \tag{33}$$

which, when substituted into (31) gives the equation

$$\lambda\Phi_{uu} + \left(2\lambda_u - \frac{\lambda\sigma_u}{\sigma}\right)\Phi_u + \left(\lambda_{uu} - \frac{\sigma_u\lambda_u}{\sigma}\right)\Phi + \lambda\sigma^2\Phi = 0 \tag{34}$$

Now, we rewrite (26) as

$$\Phi_{uu} + \sigma^2\Phi = 0 \tag{35}$$

where σ^2 is defined according to

$$\sigma^2\Phi = k^2 J\left(\Phi + k^{-2}J^{-1}\Phi_{vv}\right) \tag{36}$$

Noting that (35) contains no single derivatives of Φ, we require the coefficient of Φ_u in (34) to be zero and obtain

$$\lambda = \sigma^{1/2} \tag{37}$$

and

$$\Phi_{uu} + \lambda \left[\left(\lambda^{-2} \lambda_u \right)_u \right] \Phi + \lambda^4 \Phi = 0. \tag{38}$$

The higher order terms (second derivatives of λ with respect to u and terms which are quadratic in λ_u) may be neglected to recover (35) from (38). Using (37) in (32) then gives

$$\left(\lambda \Phi^+ \right)_u = i \lambda^3 \Phi^+. \tag{39}$$

or

$$\left((K^2 J)^{1/4} (\Phi^+ + \frac{1}{K^2 J} \Phi^+_{vv})^{1/4} \right)_u = i (K^2 J)^{3/4} (\Phi^+ + \frac{1}{K^2 J} \Phi^+_{vv})^{3/4} \tag{40}$$

Approximating the operators in (40) using the first two terms of the binomial expansion (following Booij, 1981) gives the parabolic model equation

$$\left((K^2 J)^{1/4} (\Phi^+ + \frac{1}{4K^2 J} \Phi^+_{vv}) \right)_u = i (K^2 J)^{3/4} (\Phi^+ + \frac{3}{4k^2 J} \Phi^+_{vv}) \tag{41}$$

Carrying out the derivatives then gives (where the + superscript has been dropped)

$$\begin{aligned} \Phi_u + \left(2KJ^{1/2} \right)^{-1} \left(KJ^{1/2} \right)_u \Phi - \frac{3}{8} \left(K^2 J \right)^{-3/2} \left((K^2 J)^{1/2} \right)_u \Phi_{vv} + (4K^2 J)^{-1} \Phi_{uvv} & \\ = iKJ^{1/2} \Phi + \frac{3i}{4} \left(KJ^{1/2} \right)^{-1} \Phi_{vv} & \quad (42) \end{aligned}$$

Finally, an equation for the amplitude $A(u,v)$ follows by using the substitution (27) with $J = J_0$ to obtain

$$\begin{aligned} 2iKJ^{1/2} A_u + 2KJ^{1/2} \left(KJ^{1/2} - K_0 J_0^{1/2} \right) A + i \left(KJ^{1/2} \right)_u A + \left\{ \frac{3}{2} - \frac{1}{2} \left(\frac{K_0^2 J_0}{K^2 J} \right)^{1/2} \right\} A_{vv} & \\ - \frac{3i}{4K^2 J} \left(KJ^{1/2} \right)_u A_{vv} + \frac{i}{2KJ^{1/2}} A_{uvv} = 0 (43) & \end{aligned}$$

This approximation has been referred to as the higher-order or large-angle approximation in the literature. Kirby (1986) has shown that equations of this form are the next higher-order approximation beyond the level of equation (28) in a consistent perturbation expansion. The large-angle model equations developed in the following two sections are all contained in (43) in principle.

3 Waves Between Diverging Breakwaters

As a first example, we consider the geometry shown in Figure 1, along with the coordinate mapping, $w = \ln(z/r_0)$, where $w = u + i\,v$ and $z = x + i\,y$ are complex variable representations of the coordinates. The entrance to the breakwaters lies on the circle, r_0 and between lines of constant θ, which represent lateral boundaries in an $\{r, \theta\}$ domain, with waves assumed to propagate principally in the $+r$ direction.

3.1 The Coordinate Transformation and Lowest Order Model

The most natural choice of a coordinate system from a physical point of view is the polar transformation

$$\begin{pmatrix} x \\ y \end{pmatrix} = r \begin{pmatrix} \cos\theta \\ \sin\theta \end{pmatrix}, \quad \begin{pmatrix} r \\ \theta \end{pmatrix} = \begin{pmatrix} (x^2+y^2)^{1/2} \\ \tan^{-1}(y/x) \end{pmatrix} \tag{44}$$

which relates $\{r, \theta\}$ to a Cartesian reference frame with a common origin. However, a more appropriate choice of coordinates, which represents a true conformal map, is

$$\begin{pmatrix} x \\ y \end{pmatrix} = r_0 \mathrm{e}^u \begin{pmatrix} \cos v \\ \sin v \end{pmatrix}, \quad \begin{pmatrix} u \\ v \end{pmatrix} = \begin{pmatrix} \ln(r/r_0) \\ \theta \end{pmatrix} \tag{45}$$

with the domain $(r_0 \le r \le \infty)$. The first representation can also be written as $z = r_0\,\mathrm{e}^w$. The Jacobian of this transformation is

$$J = r_0^2\,\mathrm{e}^{2u} \tag{46}$$

We consider only the case of a flat bottom, so that $K = k$. Substituting into the simple parabolic approximation (30) gives

$$2ikr_0\,\mathrm{e}^u A_u + ikr_0\,\mathrm{e}^u A + A_{vv} = 0 \tag{47}$$

To find the polar representation, we then use the change of variables

$$r = r_0\,\mathrm{e}^u; \qquad \theta = v \tag{48}$$

from both (44) and (45), and obtain the lowest-order parabolic model in polar coordinates:

$$2ikr^2 A_r + ikrA + A_{\theta\theta} = 0 \tag{49}$$

Solutions $A(r,\theta)$ of (49) have the property of decaying like $r^{-1/2}$ as $r \to \infty$, consistent with the radial decay of emissions from a point source in two dimensions. It is convenient in some applications to introduce the further transformation

$$B = r^{1/2} A \tag{50}$$

which isolates the radial decay factor. Substitution of (50) in (49) gives the alternate model

$$2ikr^2 B_r + B_{\theta\theta} = 0 \tag{51}$$

Either (49) or (51) is to be solved in a domain $\{r_0 \le r \le \infty; -\theta_a \le \theta \le \theta_b\}$.

3.2 An Alternate Direct Derivation in Polar Coordinates

The parabolic models contain the assumption that $|A_{uu}| \ll |\mathrm{e}^u A_u|$, which may be deduced directly from (7) using the given coordinate trnasformations. This assumption needs closer inspection in order to interpret its meaning. Consider a direct derivation of (49) from a polar coordinate form of the Helmholtz equation, given by

$$r^2 \eta_{rr} + r\eta_r + \eta_{\theta\theta} + (kr)^2 \eta = 0 \tag{52}$$

Assuming η to be of the form

$$\eta = A(r,\theta)\mathrm{e}^{ikr} + \text{complex conjugate} \tag{53}$$

and substituting (53) in (52) then gives

$$r^2 A_{rr} + r(2ikr + 1)A_r + ikrA + A_{\theta\theta} = 0 \tag{54}$$

The parabolic approximation is constructed by neglecting second derivatives in the propagation direction in comparison to second derivatives in the transverse direction; however, an asymptotic analysis in the present case indicates that this may only be done consistently in a region $kr >> 1$, far from the singularity at $r = 0$. Solutions of (52) have singular points at the origin $r = 0$; the classic example is that of the radially-symmetric case $(\partial/\partial\theta \equiv 0)$ which reduces (52) to a Bessel's equation of order zero. The well-known solution representing a cylindrical wave propagating to large r is

$$\eta(r) = aH_0^1(kr) \tag{55}$$

where H_0^1 is the Hankel function of first kind and order zero. Using the asymptotic form for large values of kr gives

$$\eta(r) \sim a\sqrt{\frac{2}{\pi kr}}\,\mathrm{e}^{i(kr-\pi/4)} \tag{56}$$

This may be arranged into the form of equation (53), giving

$$\eta(r) \sim \left\{\frac{2a^2}{\pi k}e^{-\frac{i\pi}{2}}\right\}^{1/2} r^{-1/2}\mathrm{e}^{ikr} = A(r)\mathrm{e}^{ikr} \tag{57}$$

where the bracketed term is essentially arbitrary due to free choice of the amplitude a. It is then easy to verify that $A(r) = a'r^{-1/2}$ is a solution of a reduced form of equation (54) given by

$$2ikr^2A_r + ikrA = 0 \tag{58}$$

and thus the neglect of the term unity in the coefficient $(2ikr + 1)$ in (54) is required in order to maintain consistency when A_{rr} is neglected. This then recovers (49), which is then valid only in the region $kr \gg 1$.

A comparison of the two derivations of (49) used here indicates that the assumption $A_{uu} \ll A_{vv}$ may only be applied consistently in regions which are asymptotically far from singularities in the coordinate mapping, or here, in the asymptotic far field of the Hankel function solution. This is not a strong restriction practically, since kr accumulates by a value of 2π over each wavelength, and hence the start of the computational domain may be as close as one or two wavelengths from $r = 0$.

An analytic solution of this parabolic model for the case of oblique incidence in a symmetric breakwater configuration (Figure 2) is given in Appendix B. In practice, it is faster to obtain numerical results than to evaluate the Bessel functions in the solution. A numerical approach also allows for the inclusion of wave nonlinearity, absorbing boundaries, and more complex breakwater configurations. We thus concentrate on numerical results below.

3.3 Large-angle Model in Polar Coordinates

Using dimensionless (u, v) coordinates defined according to (45), we obtain the higher-order approximation from (43);

$$2ikA_u + ikA + \frac{1}{r_0 \mathrm{e}^u} A_{vv} - \frac{3i}{4kr_0 \mathrm{e}^u} A_{vv} + \frac{i}{2kr_0^2 \mathrm{e}^{2u}} A_{uvv} = 0 \tag{59}$$

Adopting the transformation $r = r_0 \mathrm{e}^u, \theta = v$ further gives

$$2ikr^2 A_r + ikrA + \left(1 - \frac{3i}{4kr}\right) A_{\theta\theta} + \frac{i}{2k} A_{r\theta\theta} = 0 \tag{60}$$

Eq.(60) represents the higher-order correction to the model equation (49). The corresponding equation for the envelope function B defined by (52) is given by

$$2ikr^2 B_r + \left(1 - \frac{i}{kr}\right) B_{\theta\theta} + \frac{i}{2k} B_{r\theta\theta} = 0 \tag{61}$$

Forms essentially equivalent to (60) or (61) have been given by Hill (1986) and others for underwater acoustics applications. Equations (60) and (61) are not solvable by simple separation of variable method, and hence recourse must be made to numerical solution techniques.

3.4 Comparison to the Exact Result

For the linear problem, the parabolic models can be compared to the exact solution. The governing Helmholz equation (9) is recast into polar coordinates, so that the problem is separable.

$$\Phi_{rr} + \frac{1}{r}\Phi_r + \frac{1}{r^2}\Phi_{\theta\theta} + k^2\Phi = 0 \tag{62}$$

An assumed solution for this equation which satisfies a no-flow boundary conditions at $\theta = \pm\theta_\ell$ is

$$\Phi = F(r) \cos \beta_n (\theta + \theta_\ell) \qquad \text{for } n = 0, 1, 2, 3, \ldots \tag{63}$$

where

$$\beta_n = \frac{n\pi}{2\theta_\ell} \tag{64}$$

For cases when the solutions are symmetric with the channel centerline ($\theta = 0$), the odd values of n can be neglected.

Substituting the assumed solution into the governing equation (62) gives Bessel's equation for $F(r)$. Its solutions are

$$F(r) = H_{\beta_n}^{(1)}(kr), n = 0, 1, 2, \ldots$$

The Hankel functions of the first kind guarantee outgoing waves as $r \to \infty$.

The final solution is then written as

$$\Phi(r, \theta) = \sum_{n=0}^{\infty} a_n H_{\beta_n}^{(1)}(kr) \cos \beta_n(\theta + \theta_\ell) \tag{65}$$

The values of the unknown coefficients a_n are found from the initial condition at $r = r_0$, which is prescribed as a function of θ:

$$\Phi(r_0, \theta) = G(\theta)$$

Using the orthogonality of the cosines over the range $-\theta_\ell \leq \theta \leq \theta_\ell$, we have

$$a_m = \frac{\epsilon_m \int_{-\theta_\ell}^{\theta_\ell} G(\theta) \cos \beta_m(\theta + \theta_\ell) d\theta}{2\theta_\ell \, H_{\beta_n}^{(1)}(kr_0)} \qquad \text{for } m = 0, 1, 2, 3, \ldots \tag{66}$$

Here, ϵ_m is unity for $m = 0$, and 2 otherwise. For the case of a plane wave train entering into a diverging channel centered about $\theta = 0$, $G(\theta) = \exp(ikr_0 \cos \theta)$, corresponding to normal incidence. The result (66) may be expressed as a series of Bessel functions, as in (B5) - (B6).

Figures 3 and 4 show a comparison between the exact solution (65) and results for the small-angle and large-angle parabolic models. The wave condition corresponds to the experimental condition considered in Section 3.6. Figure 3 shows the distribution of wave amplitude $a(r, \theta)$ along three lines of constant distance r from the coordinate origin. The results are normalized by a_0, the incident wave amplitude. At $r/r_0 = 1.38$, the exact solution shows a rapid diffraction of wave energy into the shadow zone behind the diverging breakwaters. On the other hand, diffraction effects in the small-angle model are relatively slow, and a wide region of constant amplitude, indicating the undistorted incident wave, is seen. For this geometry, the large angle model corrects about half of the error between the small-angle approximation and exact solution, and still leaves qualitative as well as quantitative differences between model and exact solutions. In particular, the large dip in amplitude at the centerline, predicted by the exact solution, may be seen in the laboratory data in Figure 6. Neither parabolic model is able to predict this dip.

At greater r values, the disagreement between the large angle model and the exact solution is reduced, although there are still differences in the form of the wave amplitude distribution. Large discrepancies between the small-angle and exact solutions remain, however, and the small-angle model does not successfully reproduce the exact solution in the far field of the breakwater gap for any of the radii compared.

3.5 Nonlinear and Other Effects

The experiments described in the next section were carried out with the goal of determining the effect of wave nonlinearity on the diffraction process. The model equations described above may be extended to include third-order Stokes wave dispersion effects and bottom friction effects following Kirby and Dalrymple (1984) and Liu (1986). The extended parabolic approximation for frictionally damped, weakly-nonlinear Stokes waves is given by

$$\begin{aligned} 2ikA_r + \frac{ik}{r}A + \frac{1}{r^2}\left(1 - \frac{3i}{4kr}P_1\right)A_{\theta\theta} + \frac{iP_1}{2kr^2}A_{r\theta\theta} - K|A|^2A \\ + \frac{4k^3(1+i)}{\sinh 2kh + 2kh}\left(\frac{\nu}{2\omega}\right)^{1/2} A = 0 \end{aligned} \tag{67}$$

where

$$K = k^4\left(\frac{C}{C_g}\right)\left(\frac{\cosh 4kh + 8 - 2\tanh^2 kh}{8\sinh^4 kh}\right) \tag{68}$$

is an amplitude dispersion coefficient and ν is the kinematic viscosity of water. Also, $P_1 = 0$ produces the lower order approximation and $P_1 = 1$ produces the next higher order approximation. Eq. (67) may be written in finite difference form using the Crank- Nicolson method. We also consider the alteration of the simplest lateral boundary condition, $A_\theta = 0$, to include partial absorption:

$$A_\theta = ikr\alpha A, \qquad \theta = \theta_a, \theta_b \tag{69}$$

where $\alpha \rightarrow 1$ implies pure transmission of normally incident waves; see, e.g., Dalrymple (1992) for absorbing boundaries of entrance channels. In the examples considered below, it was found that laminar boundary layer damping did not have a significant effect on the computed solution (Kaku and Kirby, 1988), and this effect is not considered further here.

3.6 Comparison with Experimental Results

Kaku and Kirby (1988) have described a series of experiments which were conducted to test the application of the conformal mapping technique to the diverging breakwater geometry. Two geometries were tested, one with a flat bottom and one with a channel at the harbor entrance and extending into the harbor. A description of the flat-bottom geometry is given in Figure 5. The wave tank was $7.24m \times 7.24m$. The water depth at the wavemaker was $0.45m$ and decreased with a slope of $1:10$ up to the horizontal part, which had a water depth of $0.15m$. The wooden breakwaters, constructed from $1in$ plywood, were placed on the horizontal part. The breakwater enclosed a 90° sector with a gap of $1.74m$ width. The other ends of the breakwaters were connected to the corners of the tank so that wave propagation around the ends of the breakwaters could be prevented. Sand, rocks and glued fiber mats were placed at the end-wall and the corners of side-wall and breakwaters in order to damp reflected waves inside and outside the breakwaters. A flap-type single paddle wavemaker generated the incident waves, whose direction was normal to the gap. A polar coordinate grid was drawn on the bottom. Each breakwater was placed on a line of constant θ, and the origin of the coordinates was on the horizontal part.

Sample stations were then established at fixed locations on the (r, θ) grid. Wave records were obtained at each predetermined sampling station using capacitance-type wave gages mounted on steel tripods. The analog signal from the wave gage was converted into a digital signal by means of an A/D converter driven by a MICRO PDP-11 digital computer. The computer also controlled the measuring system, including calibration of gages, computation of calibration coefficients by least-square method, timing the sampling frequency and period, and storing the data into a specific file.

Because of the limited size of the tank, some physical effects caused by the tank boundaries such as cross-wise re-reflected waves and currents on the down wave side of the breakwaters were generated by the incident waves and often grew with time. A modulation of the incident wave amplitude, possibly due to a complex motion of water behind the wave maker, was also observed several minutes after turning on the wave maker. Finally, we note that several of the experiments were run with incident wave steepnesses large enough to promote the onset of Benjamin-Feir sideband instabilities. As a result of these difficulties, sampling was done only within the first minute of each run. Up to five minutes was then allowed between two consecutive samples in order to let the water calm down. A $20Hz$ sampling frequency was chosen for each sample. The sampling period was selected between $15sec$ and $30sec$, depending on the period of the incident waves and on the location of the sampling station. The stations far from the gap and near the breakwater sometimes required a longer sampling period due to the presence of relatively larger amplitude modulations relative to the incident wave amplitude. In analysing the data records, a Fourier transform was applied to isolate the fundamental frequency band, and then wave amplitudes were calculated for each station.

Because of the difficulties noted with long wave generation and re-reflection within the harbor, we show the results of only one test here. The results shown here are typical of the range of tests done; no one test showed a greater degree of systematic agreement or disagreement with model results than the chosen one. The test chosen here had the largest value of wave steepness of all the tests conducted, and hence provides a stronger test of the nonlinear aspects of the model equation. For this test, a wave period of $T = 0.49s$ and amplitude of $a_0 = 0.017m$ were used, leading to an initial wave steepness $ka_0 = 0.288$. The resulting data are compared to numerical results in Figure 6. The numerical grid was uniformly discretized over θ, with the 90° sector divided into 100 steps. Discritization in u was distorted in order to obtain equal steps in physical distance r, and 100 steps were taken from an initial radius $r/r_0 = 1.23$ to a final radius $r/r_0 = 2.5$.

In general, for the constant depth case, results of the higher-order approximation agree well with laboratory data. On the section $r/r_0 = 1.38$, the laboratory data indicate that diffraction effects occur at smaller θ values than the values predicted by the lowest-order model and are well predicted by the higher-order approximation. On the section $r/r_0 = 1.87$, the higher-order approximation predicts the wave amplitude very well within $0^\circ \leq \theta \leq 20^\circ$ and slightly underpredicts the laboratory data at $\theta = 30^\circ$ and $\theta = 40^\circ$. On the section $r/r_0 = 2.2$, reasonable agreement with the higher-order nonlinear or lowest-order nonlinear approximation is seen, although the differences between the different approximations are reduced at this distance into the harbor.

The results here are indicative of the general level of agreement between data and numerical prediction found in the data set as a whole. Experimental errors in the data set make it difficult to clearly determine that the large-angle approximation is out-performing the small-angle approximation in all cases. In this regard, the results of Section 3.4 should be taken as the primary indication that the large angle model provides a better approximation.

4 Circular Channel

As an alternative example, consider the case of waves in a curved channel, as shown in Figure 7. Here, the wave field is prescribed at the entrance of the channel, which has a width of $r_2 - r_1$. The mapping is not the same as in the diverging channel section, as we want to keep u as the propagation direction; now $z = -r_1 \mathrm{e}^{iw^*}$, or $w^* = -i \ln iz/r_1$. Alternatively, we can write it

$$\begin{pmatrix} x \\ y \end{pmatrix} = r_1 \mathrm{e}^v \begin{pmatrix} \sin u \\ -\cos u \end{pmatrix}, \quad \begin{pmatrix} u \\ v \end{pmatrix} = \begin{pmatrix} \theta + \pi/2 \\ \ln(r/r_1) \end{pmatrix} \tag{70}$$

For this transformation, $J = -r_1^2 \mathrm{e}^{2v}$, which is now a function of v, not u, as in (46). The transformed domain, as shown in Figure 7, ranges from $0 \le v \le \ln(r_2/r_1), 0 \le u$.

4.1 Parabolic Approximation

The small and large angle parabolic models are the same as used before: (28) and (43). The value of J_0 used is that at the midpoint of the channel, where $v = \ln[(r_1 + r_2)/(2r_1)]$. Results of parabolic model calculations are compared to an exact solution in Section 4.3.

4.2 Exact Solution

Again, the polar form of the Helmholz equation (62) is used, except that in this example, the radial direction is across the channel and the θ direction corresponds to the channel axis. The assumed form of the progressive wave solution is now

$$\Phi = F(r)\, \mathrm{e}^{i\gamma\,(\theta + \frac{\pi}{2})} \tag{71}$$

where γ is not necessarily an integer. The resulting Bessel equation has a solution in terms of Bessel functions of order γ:

$$F(r) = aJ_\gamma(kr) + bY_\gamma(kr) \tag{72}$$

where a and b are unknown constants. There are two no-flow conditions to be satisfied at the sidewalls,

$$F_r = 0 \text{ at } r = r_1,\ F_r = 0 \text{ at } r = r_2, \text{ for } \theta > \pi/2 \tag{73}$$

The first condition relates a to b,

$$a = -b\,\frac{Y'_\gamma(kr_1)}{J'_\gamma(kr_1)} \tag{74}$$

where the primes denote derivatives with respect to kr. The second no-flow condition establishes a condition on γ.

$$Y'_\gamma(kr_1)J'_\gamma(kr_2) - J'_\gamma(kr_1)Y'_\gamma(kr_2) = 0 \tag{75}$$

There are only a finite number of discrete values of $0 < \gamma < kr_2$ for which this condition is satisfied. The total solution is given by

$$\begin{aligned} \Phi &= \sum_n a_n \left[Y'_{\gamma_n}(kr_1)J_{\gamma_n}(kr) - J'_{\gamma_n}(kr_1)Y_{\gamma_n}(kr)\right]\, \mathrm{e}^{i\gamma_n(\theta+\pi/2)} && (76)\\ &= \sum_n a_n F_n(r)\, \mathrm{e}^{i\gamma_n(\theta+\pi/2)} && (77) \end{aligned}$$

Each function $F_n(r)$ is orthogonal over the range $r_1 \leq r \leq r_2$ with weight $1/r$, from the Sturm-Liouville theory. Therefore, at the beginning of the channel, $\theta = -\pi/2$, the initial condition is used to determine the values of a_n.

$$\sum_n a_n(Y'_{\gamma_n}(kr_1)J_{\gamma_n}(kr) - J'_{\gamma_n}(kr_1)Y_{\gamma_n}(kr)) = G(r) \tag{78}$$

which, using the orthogonality condition, yields

$$a_n = \frac{\int_{r_1}^{r_2} \frac{F_n(r)G(r)}{r}\,dr}{\int_{r_1}^{r_2} \frac{F_n^2}{r}\,dr} \tag{79}$$

In the following examples, the initial condition is a wave train with constant amplitude across the channel, or $G(r) = 1$. This solution has been previously discussed by Rostafinski (1976) in the context of acoustics.

4.3 Comparison of the Parabolic Models to the Exact Solution.

The parabolic model and exact solutions are compared here for a particular choice of geometry and wave conditions. Only linear waves are considered, since the exact solution does not have a nonlinear counterpart. The channel lies between two radii, $r_1 = 75m$ and

$r_2 = 200m$, and covers a 180° arc. Plane waves with a uniform amplitude across the channel are imposed at the entrance. The water depth is uniform with $h = 10m$, and the wave period is taken to be $T = 4s$.

Figure 8 shows a plot in physical coordinates of the instantaneous water surface specified by the exact solution, with a plane wave entering at the bottom right of the figure and propagating around teh bend in a counter-clockwise direction. A zone of reflection develops along the outside wall, with the wave height along the wall reaching a maximum at about 60° from the entrance. At the same time, a shadow zone with a diffracted wave field develops on the inside wall as the wall bends away from the incident wave. The region from 60° to 90° is dominated by an intersecting wave pattern resulting from the superposition of the incident wave and the wave reflected off the outer wall. Beyond this angle, the wave field is more organized with the exception of a complex re-reflection pattern which develops again along the outer wall.

In Figure 9, we show a comparison of the surface elevation variation along the outer wall. The solid line shows the exact solution. The small-angle parabolic model solution is indicated by the dash-dot line. This line begins to diverge from the exact solution around the first maximum in the wave height, after which there are strong dissagreements (both in amplitude and phase) between the two results. The large-angle model, whose results are indicated by the dashed line, shows a much stronger agreement with the exact solution, maintaining fairly accurate phase and amplitude around the entire 180° sector.

4.4 Nonlinear effects.

Waves entering a gradual channel bend are initially incident at a very small angle to the outer channel wall. This angle increases from zero to large values as distance around the bend increases. In the region of initial, small incidence angle, it is known that the regular reflection pattern predicted by linear theory is replaced, in nonlinear theory, by the appearance of a Mach stem, which is an analog to Mach reflection in shock wave dynamics. The stem consists of a section of wave crest oriented perpendicular to the vertical boundary wall, beyond which a more standard reflection pattern develops. For the case of Stokes waves in deep or intermediate water depth, the phenomenon has been studied by Yue and Mei (1980). In order to illustrate the Mach stem effect in the present context, we show a series of calculations in Figures 10 through 12 which correspond to a linear solution and to nonlinear solutions with wave steepness $ka_0 = 0.2$ and 0.3. The nonlinear model is again an extension of the results in Kirby and Dalrymple (1984). The computations are based on the same set of parameters as in the previous section. Results are plotted in the u (or θ)-v plane. The series of figures shows a gradual weakening and displacement down the channel of the principal reflected wave crest, which leaves the channel wall near $\theta = 45°$ in the linear wave case. The width of the initial wave crest along the outer channel wall increases markedly with increasing nonlinearity, which is the principal manifestation of the Mach stem effect. In Figure 12, where the nonlinear effects are most pronounced, we see that the growth of the wide stem wave is repeated in each re-reflection pattern along the outer channel wall.

Figure 13 shows the evolution of wave height along the outer channel wall for the three cases shown in Figures 10-12. Increasing nonlinearity causes a reduction of maximum wave height in the stem wave region, and displaces the maxima progressively further downwave, as mentioned in the previous paragraph. Figure 14 shows the cross-channel wave height at the point along the channel where the first maximum in stem wave height occurs. Increasing nonlinearity leads to lower stem waves with wider crests perpendicular to the wall, as has also been previously noted.

Nielsen (1962) studied a case very similar to the one studied here. In Nielsen's experiments, a Mach stem is induced along an initially straight wall, which then is smoothly matched to a radial wall section. As the Mach stem propagates around the wall, the incident wave becomes more oblique and the Mach reflection is replaced by regular reflection and separation of a reflected wave train from the wall. We consider here the particular case with parameters $T = 0.2813s, kh = 2.51327$, and $ka_0 = 0.226$. The outer radius of the concave wall is 1.016m. The corresponding Figure 35 from Nielsen (1962) is shown in Figure 15. The figure shows the development of a Mach stem and a hexagonal wave pattern along the outer wall, with subsequent separation of the reflected wave from the wall around $\theta = 55°$. This reflection is qualitatively similar to the pattern seen in Figures 10-12. Figure 16 shows the results of a numerical calculation using the parameters above and an inner radius $r_1 = 0.05m$. Since the initial straight wall section in Nielsen's experiment is not modelled, the comparisons here are only qualitative. The results indicate a very similar pattern, however, with the apparent growth of the Mach stem up to $\theta = 45°$, and subsequent separation of the reflected wave from the wall and the appearance of a quiet zone along the wall in the region $\theta > 70°$. The hexagonal appearance of the wave field in Nielsen's picture is not reproduced in Figure 16 since the parabolic model gives only the fundamental amplitude component. Reproduction of the visual hexagon pattern requires the inclusion of the forced second harmonic components in the reconstructed water surface.

4.5 Variable Depth

In the constant depth case, it was clear that the wave crests become distorted in the channel due to the differences in travel time along the circumferential paths taken by the waves. It is possible, however, to chose a depth for which the wave phase speed varies across the channel accounting for the longer travel distance at the outer circumference. Examining the parabolic equation for this case (30), we see that the third term $\left(K^2 J - K_0^2 J(u, v_0)\right) A$ is responsible for the changes in wave phase across the channel for constant values of u. If we choose a bottom variation across the channel such that the local wave number K causes this term to be zero, then the wave crests will be constant for constant values of v, or, in the real domain, there will be no phase variation with v across the channel. Therefore, for each location across the channel the depth is found from the dispersion relationship for a k given by

$$k = k_0 \sqrt{J_0 / J} \tag{80}$$

A Newton-Raphson procedure can readily solve (80) for the correct depth distribution, given k.

5 Discussion

The work done here provides an adequate foundation for the application of small and large angle parabolic approximations in distorted grids which are related to Cartesian space by a conformal transformation. It is felt that grids of this type are desirable since the scaling aspects of the resulting parabolic models are well understood. (For an example of the ambiguity arising in non-conformal cases, see Kirby, 1988). For both of the test cases considered here, the large-angle parabolic approximation (in the form developed by Booij (1981) and Kirby (1986)) provided a reasonably good prediction of the modelled wave field in comparison with more complete analytical solutions of the problem.

Although a distinct difference has been found between models based on arbitrary transformations and ones based on strictly conformal transformations, some effort should be made in the direction of almost-conformal transformations, which presumably would lead to models which differed from the present ones by terms which are in some sense small. This extension would allow for the use of the wide range of orthogonal grid generating schemes which are now available, and which do not produce strictly conformal grid structures.

Acknowledgements

This work is a result of research sponsored by NOAA Office of Sea Grant, Department of Commerce, under Grant No. NA/16RG0162-03 (Project No. R/OE-12 (RAD) and R/OE-13 (JTK)) The U. S. Government is authorized to produce and distribute reprints for governmental purposes, notwithstanding any copyright notation that may appear hereon. The authors also thank Prof. Robert Wiegel for providing the original of the photograph used in Figure 15.

Appendix A. Expressions for $\nabla^2 u$ and $\nabla^2 v$

The general form of the transformed Helmholtz equation (11) involves the expressions

$$\nabla^2 u = u_{xx} + u_{yy} \tag{A1}$$

$$\nabla^2 v = v_{xx} + v_{yy} \tag{A2}$$

For $\{x, y\}$ given in terms of $\{u, v\}$, these expressions may be written as

$$\nabla^2 u = J^{-3} \left\{ x_v \left(\beta y_{uu} - 2\gamma y_{uv} + \alpha y_{vv} \right) - y_v \left(\beta x_{uu} - 2\gamma x_{uv} + \alpha x_{vv} \right) \right\} \tag{A3}$$

$$\nabla^2 v = J^{-3} \left\{ y_u \left(\beta x_{uu} - 2\gamma x_{uv} + \alpha x_{vv} \right) - x_u \left(\beta y_{uu} - 2\gamma y_{uv} + \alpha y_{vv} \right) \right\} \tag{A4}$$

where J is given by (18). For $\{u, v\}$ conformal to $\{x, y\}$, use of the Cauchy-Riemann conditions (23) in (A3-A4) yields the results (24).

Appendix B: Analytic Solution for the Small-angle Parabolic Model for Symmetrical Breakwaters: Linear Theory

In order to allow an analytic treatment, we consider a simplification of the Figure 1 setting and take $\theta_a = -\theta_b = \theta_\ell, r_a = r_b = r_0$; we will thus study the wavefield entering the gap between a symmetric breakwater configuration shown in Figure 2. We seek a solution of (49) by separation of variables in the form

$$A = R(r) \cos \beta_n(\theta + \theta_\ell) \tag{B1}$$

which satisfies the no-flow boundary conditions at $\theta = \pm\theta_\ell$, and gives

$$2ikr^2 R' + ikrR - \beta_n^2 R = 0 \tag{B2}$$

where β_n is defined in Eq. (64).

Therefore, solving the R equation, we have

$$A(r,\theta) = \left[a_0 + \sum_{n=1}^{\infty} a_n \, \mathrm{e}^{i\left(\frac{n^2\pi^2}{2\theta_\ell^2 kr}\right)} \cos\{\beta_n(\theta+\theta_\ell)\} \right] r^{-1/2} \tag{B3}$$

The radial amplitude decay of all modes is equal to $r^{-1/2}$, the same as for a cylindrical wave front entering the domain. The remaining exponential factors in each mode are phase distortions caused by small angles of propagation with respect to the local coordinate direction.

The solution must now be matched to the initial condition at the breakwater entrance. We write the incident plane wave as

$$\begin{aligned} \eta_I &= \frac{a}{2}\mathrm{e}^{i(k\cos\theta_0 x + k\sin\theta_0 y)} + c.c. \\ &= \frac{a}{2}\mathrm{e}^{ikr_0\cos(\theta-\theta_0)} + c.c. \end{aligned} \tag{B4}$$

on $r = r_0$. The amplitude $A(r_0, \theta)$ may then be written as

$$A(r_0,\theta) = a\mathrm{e}^{ikr_0[\cos(\theta-\theta_0)-1]}, \tag{B5}$$

which must be equal to the solution within the breakwaters (B3) evaluated at r_0.

Following MacCamy and Fuchs (1954), with further reference to Abramowitz and Stegun (1972, eqs. 9.1.44-45), we may write $A(r_0, \theta)$ as

$$A(r_0, \theta) = a\mathrm{e}^{-ikr_0} \left\{ J_0(kr_0) + \sum_{m=1}^{\infty} 2(i)^m J_m(kr_0) \cos[m(\theta - \theta_0)] \right\} \tag{B6}$$

where J_m is the Bessel function of first kind and order m. The coefficients a_0, a_n and b_n may now be determined using a standard orthogonalization procedure, which yields

$$\begin{aligned} a_0 &= a r_0^{1/2} \mathrm{e}^{-ikr_0} \left\{ J_0(kr_0) + \sum_{m=1}^{\infty} \frac{2(i)^m}{m\theta_\ell} J_m(kr_0) \sin m\theta_\ell \cos m\theta_0 \right\} && \text{(B7)} \\ a_n &= 2a r_0^{1/2} e^{-i[kr_0 + n^2\pi^2/2kr_0\theta_\ell^2]} \cdot \sum_{m=1}^{\infty} (i)^m J_m(kr_0) I_{m,n}^1 \cos m\theta_0 && \text{(B8)} \end{aligned}$$

where

$$I_{m,n}^1 = \left\{ \begin{array}{ll} (-1)^n \sin m\theta_\ell \left\{ \frac{1}{(m\theta_\ell - n\pi)} + \frac{1}{m\theta_\ell + n\pi)} \right\}, & m \neq \frac{n\pi}{\theta_\ell} \\ \left\{ 1 + \frac{\sin 2m\theta_\ell}{2m\theta_\ell} \right\}, & m = \frac{n\pi}{\theta_\ell} \end{array} \right\} \tag{B9}$$

Equation (B3), together with (B7 and B8), fully specifies the linear solution for the simple parabolic case considered, and may be used to verify subsequent numerical schemes for (49).

References

Abramowitz, M. and Stegun, I. A., 1972, *Handbook of Mathematical Functions*, Dover.

Berkhoff, J. C. W., 1972, "Computation of combined refraction-diffraction", *Proc. 13th Intl. Conf. Coast. Engrng.*, ASCE, Vancouver.

Booij, N., 1981, "Gravity waves on water with non-uniform depth and current", Report 81-1, Department of Civil Engineering, Delft Univ. of Technology.

Dalrymple, R. A., 1992, "Water Wave Propagation in Jettied Channels," *Proc. 23rd Intl. Conf. Coast. Engrng,*, ASCE, Venice, 3040-3053.

Hill, R. J., 1986, "Wider-angle parabolic wave equation," *J. Acoust. Soc. Am.*, 79, 1406-1409.

Kaku, H. and Kirby, J. T., 1988, "A parabolic equation method in polar coordinates for waves in harbors," Tech. Report UFL/COEL-TR/075, Coastal and Oceanographic Engineering Department, University of Florida, Gainesville.

Kirby, J. T. and Dalrymple, R. A., 1984, "Verification of a parabolic equation for propagation of weakly-nonlinear waves," *Coastal Engineering*, 8, 219-232.

Kirby, J. T., 1986, "Higher-order approximations in the parabolic equation method for water waves," *J. Geophys. Res.*, 91, 933-952.

Kirby, J. T., 1988, "Parabolic wave computation in non-orthogonal coordinate systems," *J. Waterway, Port, Coastal and Ocean Engrg.*, 114, 673-685.

Liu, P. L.-F., 1986, "Viscous effects on evolution of Stokes waves," *J. Waterway, Port, Coastal and Ocean Eng.*, 112, 55-63.

Liu, P. L.-F., 1990, "Wave transformation", in *Ocean Engineering Science. The Sea, Volume 9, Part A*, Le Méhauté, B. and Hanes, D. M. (eds), 27-63.

Liu, P. L.-F. and Boissevain, P.L., 1988, "Wave propagation between two breakwaters," *J. Waterway, Port, Coastal and Ocean Engrg.*, 114, 237- 247.

MacCamy, R. C. and Fuchs, R. A., 1954, "Wave forces on piles: a diffraction theory," Tech. Memo, 69, Beach Erosion Board.

Nielsen, A.H., 1962, "Diffraction of periodic waves along a vertical breakwater for small angles of incidence", Tech. Rept. HEL-1-2, Institute of Engineering Research, Hydraulic Engineering Laboratory, University of California, Berkeley, CA.

Radder, A. C., 1979, "On the parabolic equation method for water wave propagation", *J. Fluid Mech.*, 95, 159-176.

Rostafinski, W., 1976, "Acoustic systems containing curved duct sections," *J. Acoust. Soc. Am.*, 60, 23-28.

Thompson, J.F., Warsi, Z.U.A. and Mastin, C.W., 1985, *Numerical Grid Generation: Foundations and Applications*, North-Holland.

Tsay, T.-K., Ebersole, B. A. and Liu, P. L.-F., 1989, "Numerical modelling of wave propagation using parabolic approximation with a boundary-fitted co-ordinate system", *Int. J. Num. Meth. Engrng.*, 27, 37-55.

Yue, D. K.-P. and Mei, C. C., 1980, "Forward diffraction of Stokes waves by a thin wedge", *J. Fluid Mech.*, 99, 33-52.

List of Figures

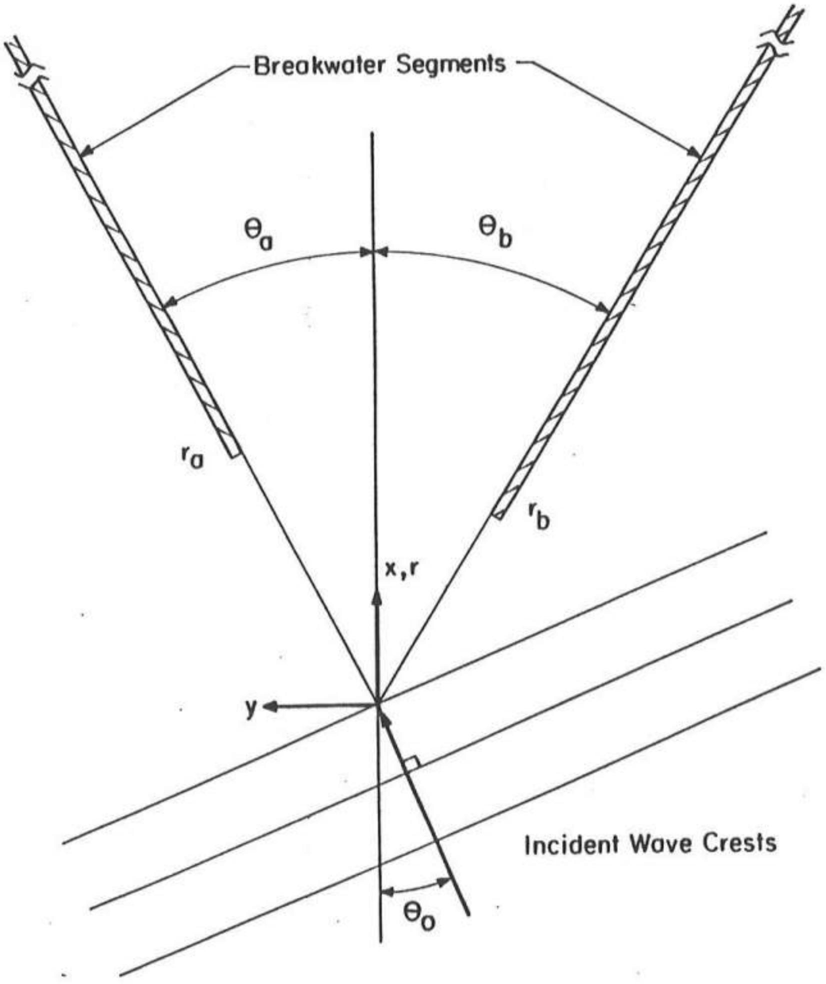

Figure 1: General configuration of diverging breakwaters

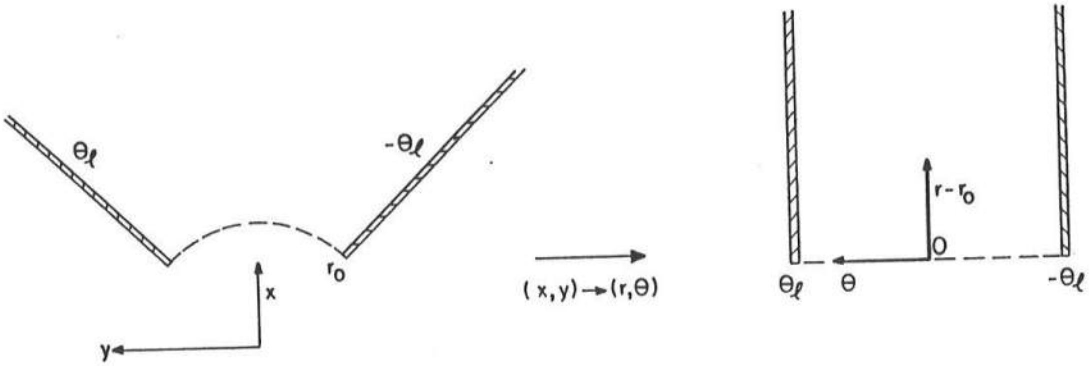

Figure 2: Symmetrical breakwater configuration for the analytic solutions in Section 3.4 and Appendix B

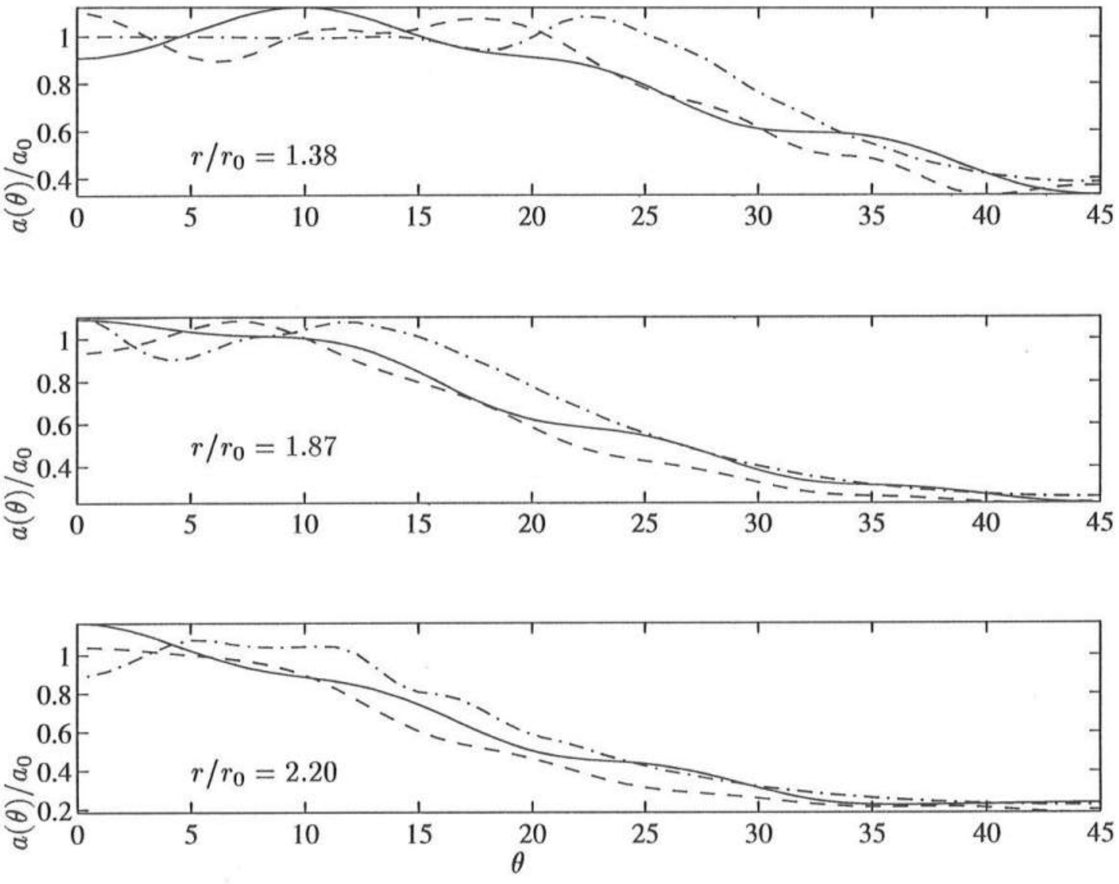

Figure 3: Comparison of normalized amplitude $a(\theta)/a_0$ along constant r lines, linear results. Solid line - exact solution (65); Dashed line - large angle parabolic model; Dashed-dot line - small angle parabolic model.

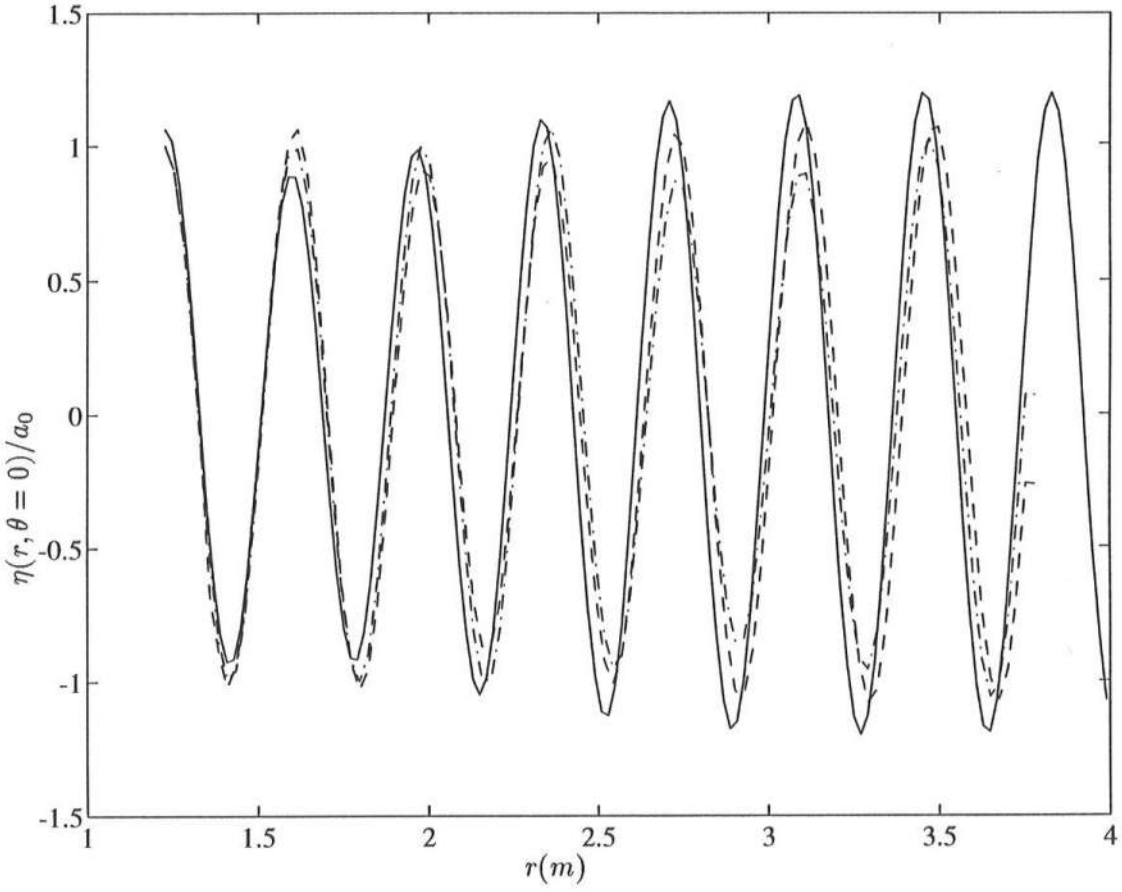

Figure 4: Comparison of normalized surface displacement $\eta(r)/a_0$ along centerline $\theta = 0$, linear results. Solid line - exact solution (65); Dashed line - large angle parabolic model; Dashed-dot line - small angle parabolic model.

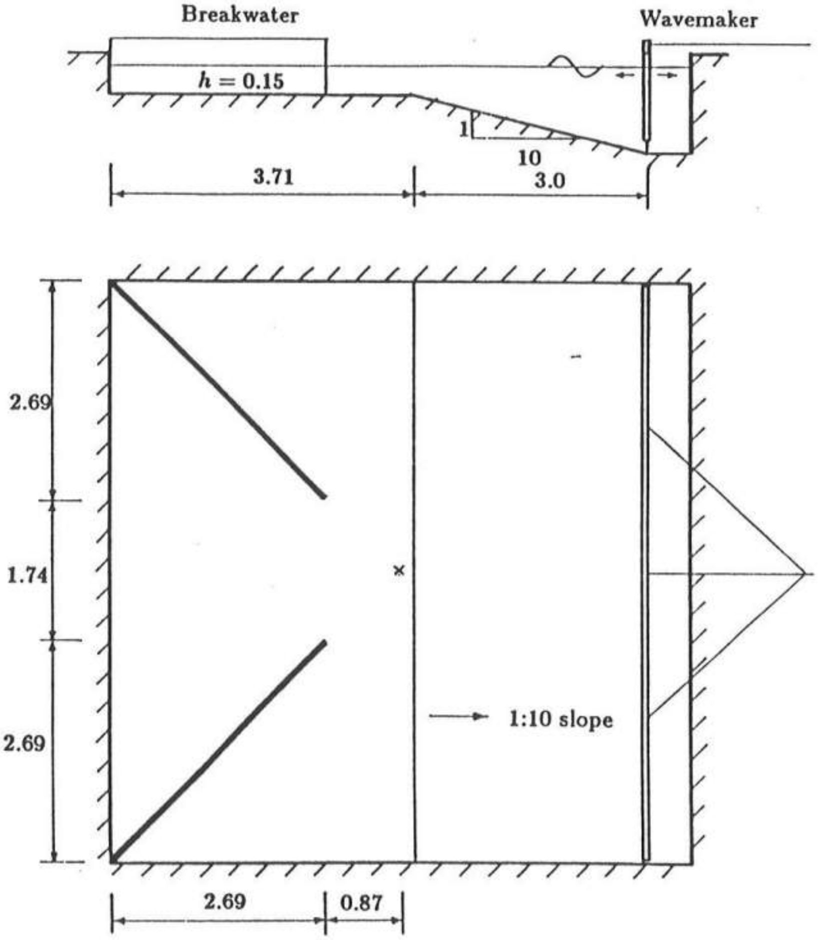

Figure 5: Experimental configuration.

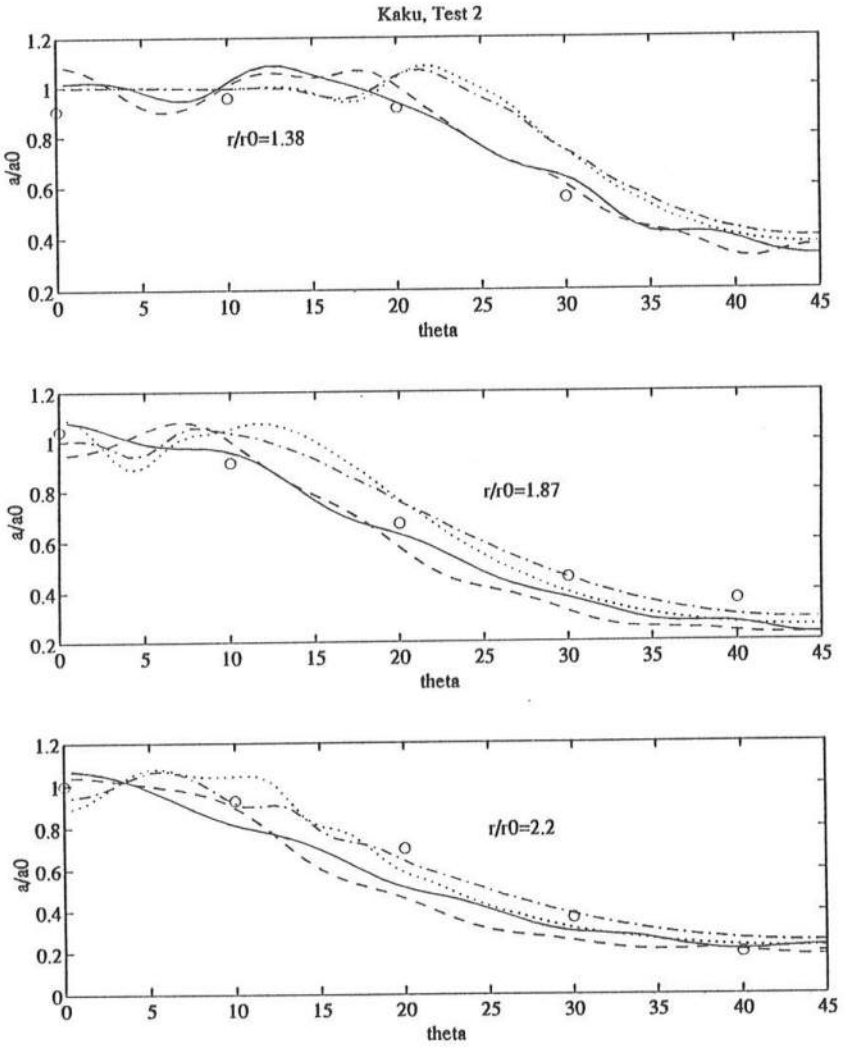

Figure 6: Comparison of numerical results and measured wave amplitudes. Circles - data. Solid line - large-angle nonlinear. Dashed line - large-angle linear. Dotted line - small-angle linear. Dash-Dot line - small-angle nonlinear.

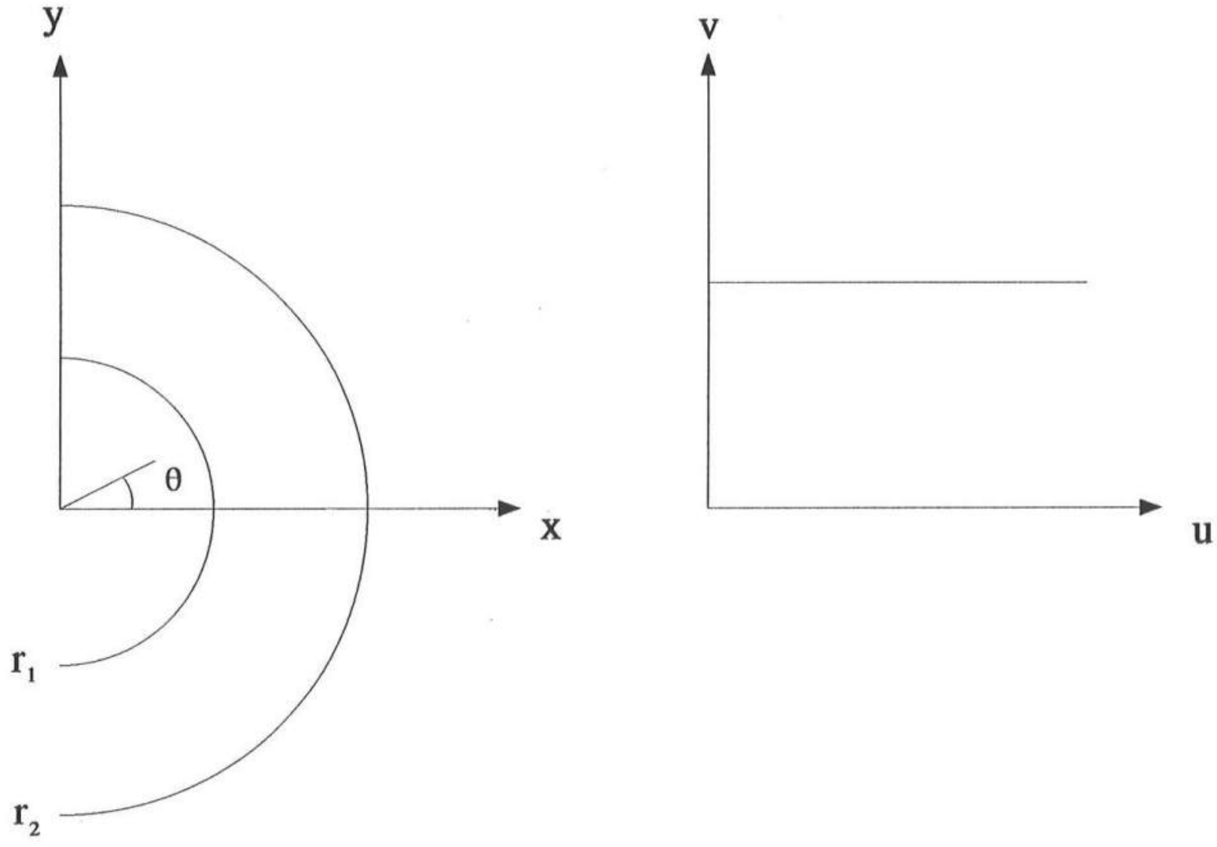

Figure 7: General configuration of circular channel

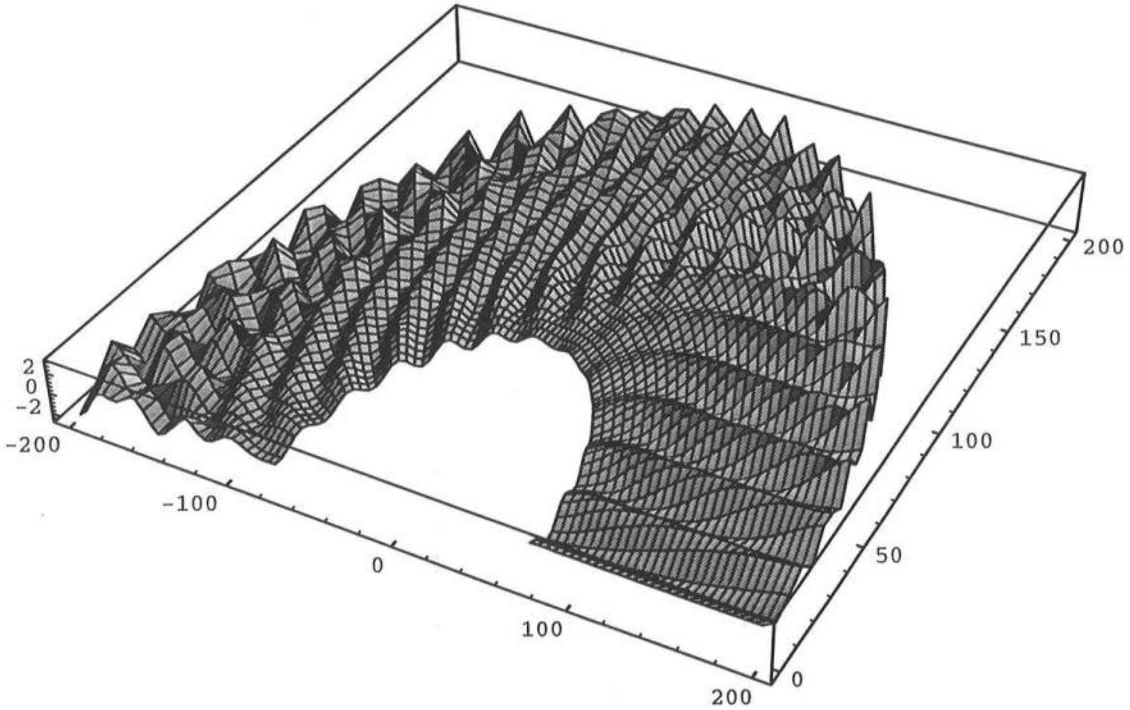

Figure 8: Exact solution in (x, y). Linear model.

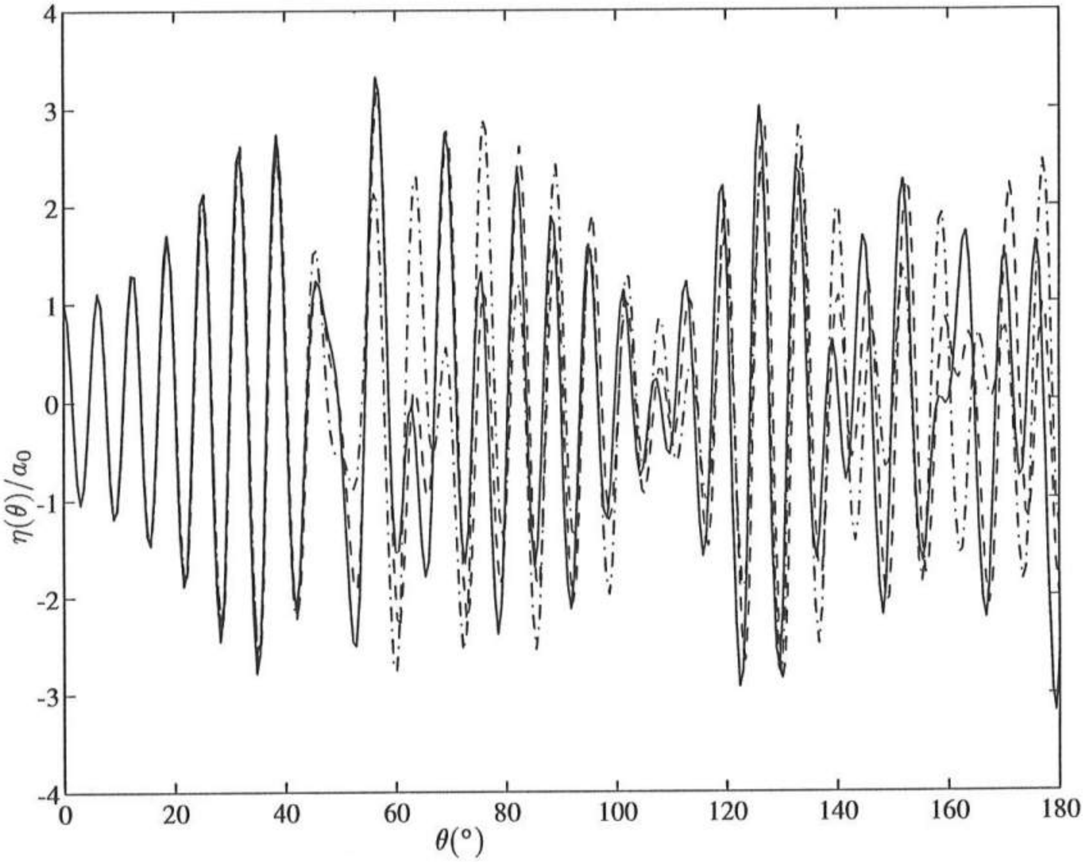

Figure 9: Comparison of normalized $\eta(\theta)$ along the r_2 wall, linear results. Solid line - exact solution (71); Dashed line - large angle parabolic model; Dashed-dot line - small angle parabolic model.

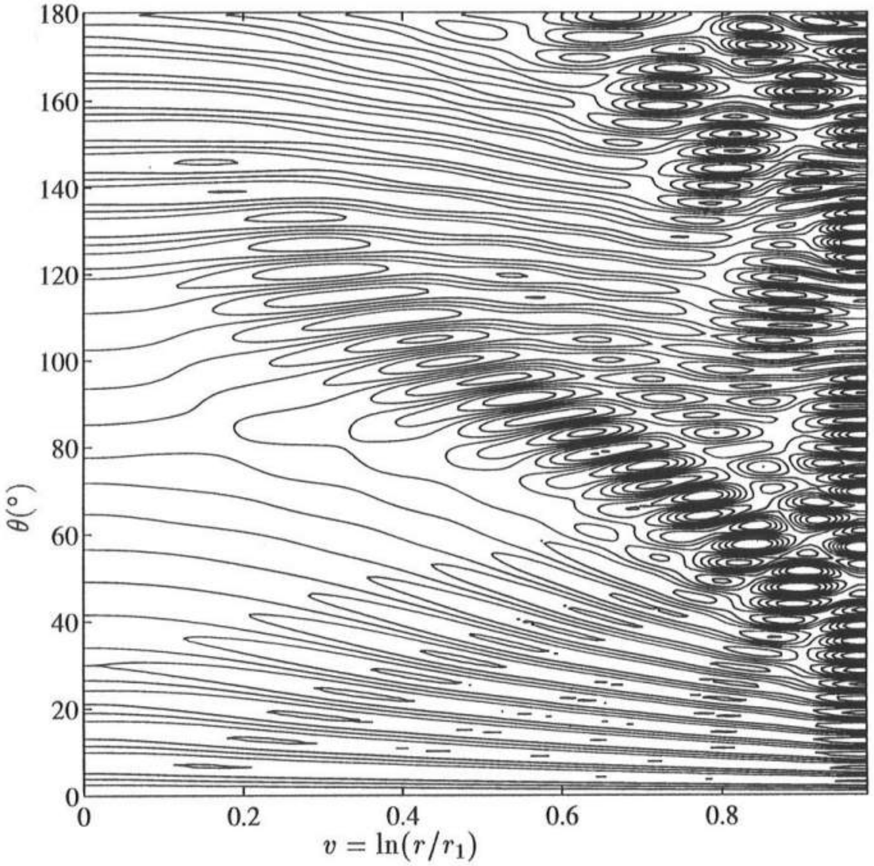

Figure 10: Solution of large angle parabolic model in (v, θ). Linear model. Plots of instantaneous water surface elevation.

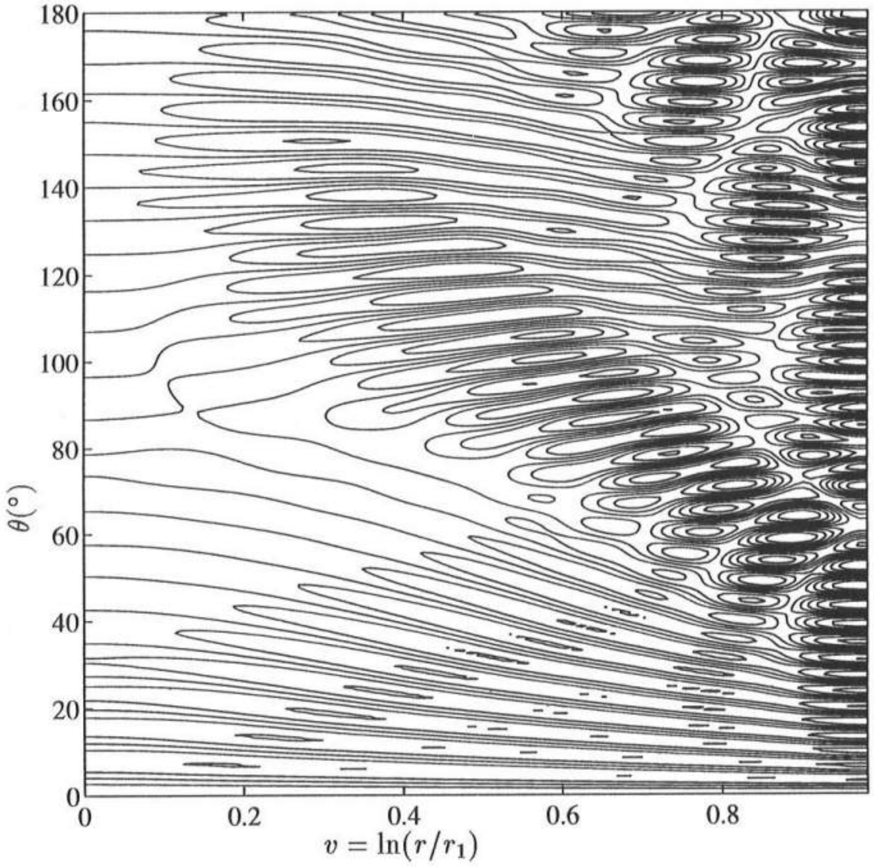

Figure 11: Solution of large angle parabolic model in (v, θ). Nonlinear model, $ka_0 = 0.20$. Plots of instantaneous water surface elevation.

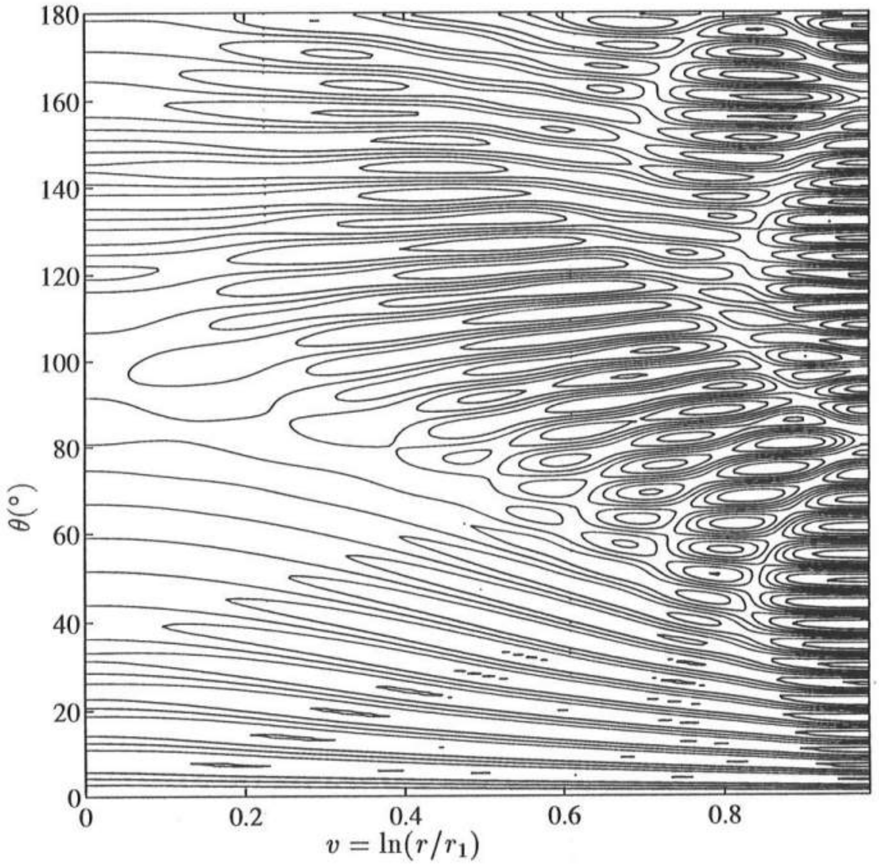

Figure 12: Solution of large angle parabolic model in (v, θ). Nonlinear model, $ka_0 = 0.30$. Plots of instantaneous water surface elevation.

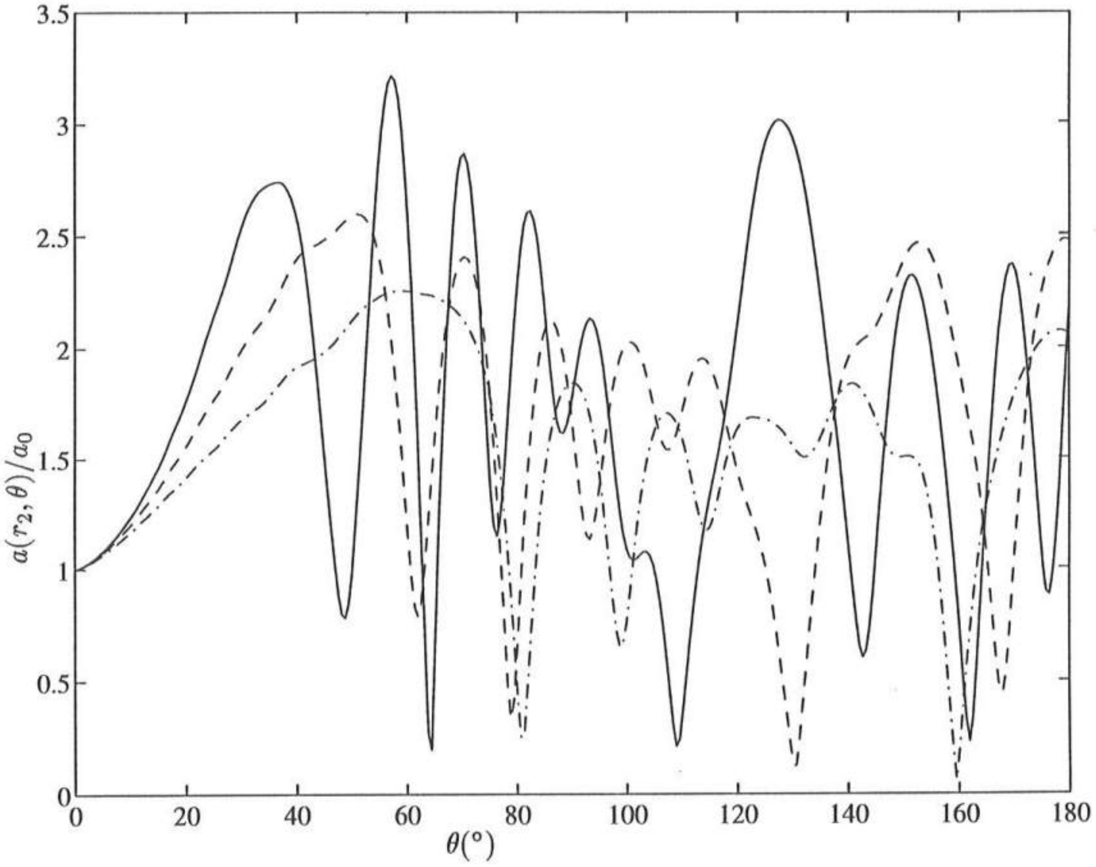

Figure 13: Amplitude of parabolic model solutions along r_2 wall. Solid line - Linear model; Dashed line - Nonlinear model, $ka_0 = 0.20$; Dash-dot line - Nonlinear model, $ka_0 = 0.30$.

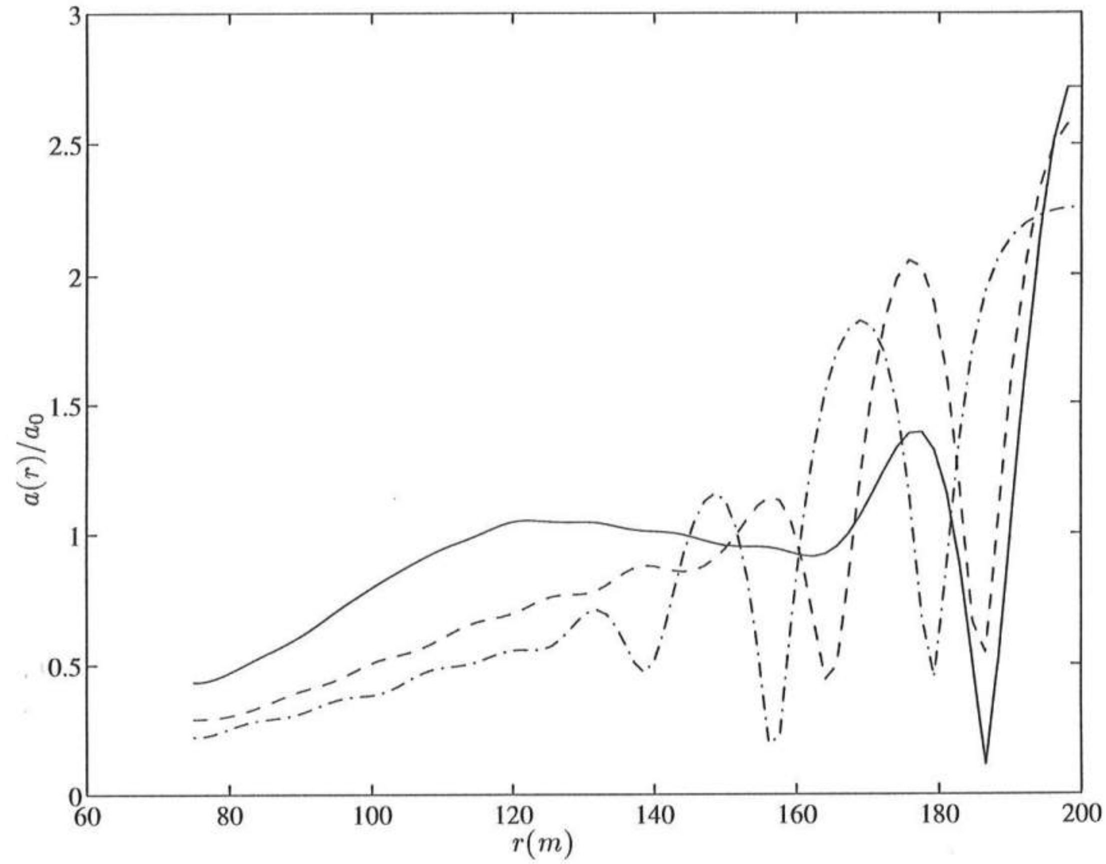

Figure 14: Amplitude of parabolic model solutions across channel at point of first maximum along channel. Solid line - Linear model, $\theta = 35°$; Dashed line - Nonlinear model, $ka_0 = 0.20, \theta = 50°$; Dash-dot line - Nonlinear model, $ka_0 = 0.30, \theta = 60°$.

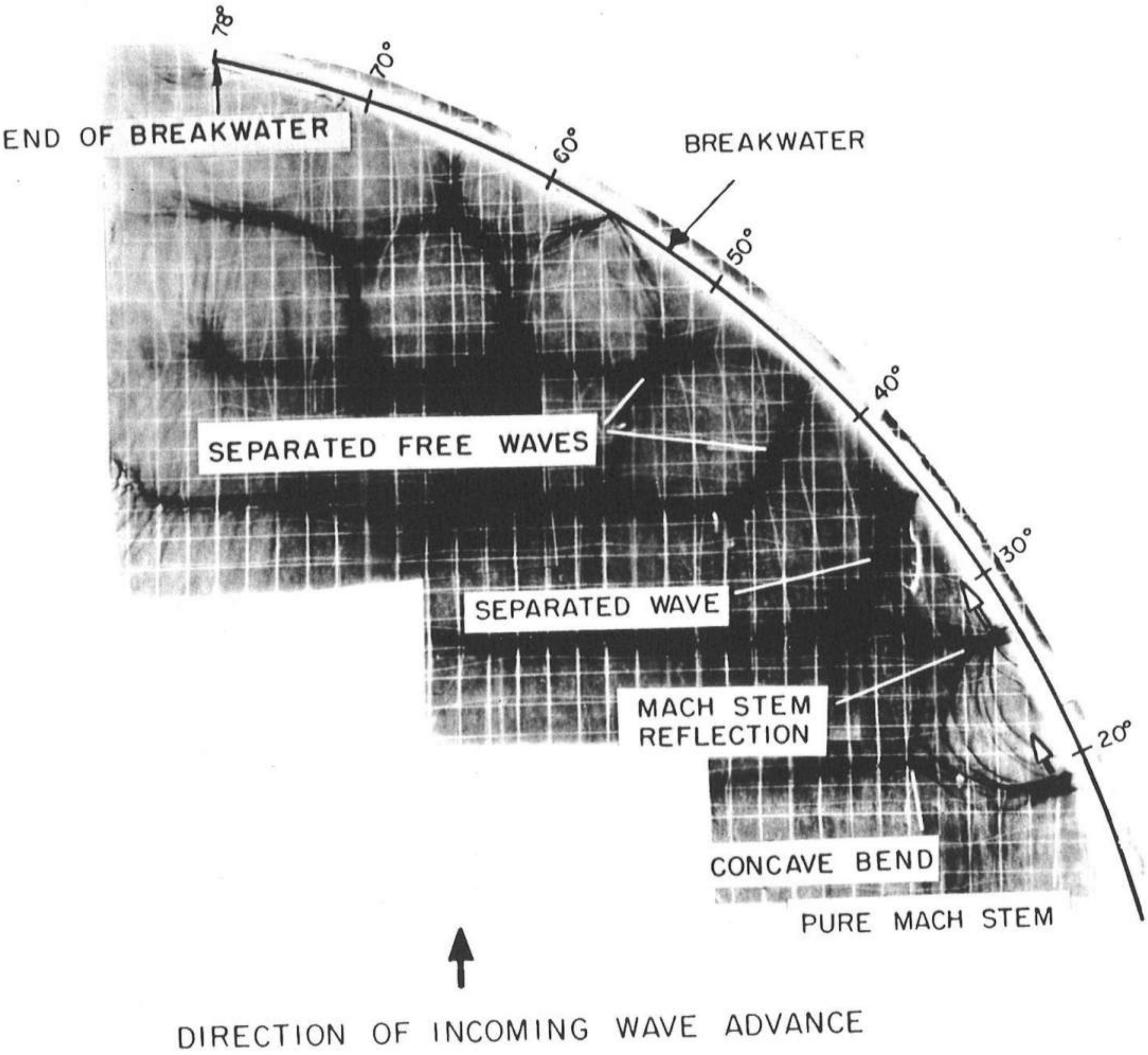

Figure 15: Wave pattern along curved breakwater: $kh = 2.513$, $ka_0 = 0.226$, $h = 4.88cm$. (from Nielsen (1962), Figure 35).

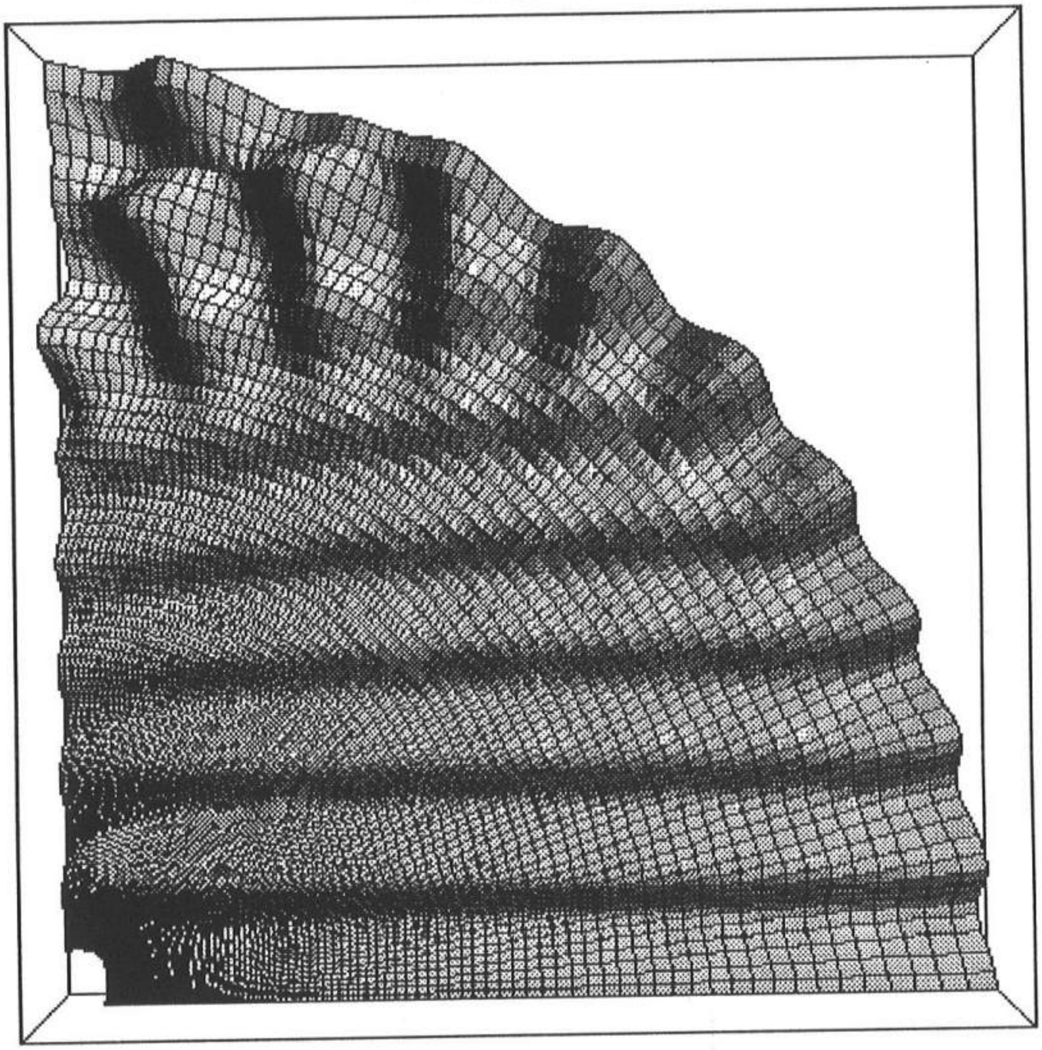

Figure 16: Qualitative comparison to the photographic result in Figure 35 of Nielsen (1962), showing wave evolution along a concave wall.